

HALE Multidisciplinary Design Optimization Part II: Solar-Powered Flying-Wing Aircraft

Dorian F. Colas* Nicholas H. Roberts[†] and Vishvas S. Suryakumar[‡]

Facebook Inc, Menlo Park, California, 94065, USA

A conceptual multidisciplinary framework is developed for the design and analysis of solar-powered, High Altitude Long Endurance (HALE) flight vehicles. Typical design features such as low wing loading and high aspect ratio imply strong inter-disciplinary couplings, in particular, aerodynamics and structures. A MultiDisciplinary Optimization (MDO) framework is therefore required to fully exploit potential couplings that may result in significant weight savings. In order to rapidly and accurately explore the design space, physics-based first principles are emphasized and reliance on historical or empirical data is minimized. In this paper (Part II), we describe how a solar-powered flying-wing configuration may be optimized using a strategy similar to that described in Part I. A key design driver in this case is the suppression of an aeroelastic phenomenon, “Body-Freedom-Flutter”, resulting from strong modal interactions due to wing sweep. Consequently, for the present study, it is shown that resulting designs are stiffness-driven as opposed to the strength-driven characteristic of conventional configurations (tail-stabilized). In addition, potential benefits of recent progress in active flutter suppression technologies are investigated.

I. Introduction

As discussed in Part I¹ of this paper series, High Altitude Long Endurance (HALE) platforms have garnered much attention, especially in recent times, with the need to improve global communication capabilities, particularly, in regions of low internet connectivity. Solar-powered airplanes offer the potential of perpetual flight with the ability to station-keep for several months. However, the stringent operating conditions, particularly during winter solstice, place demanding requirements on every aircraft subsystem. For instance, the need for long endurance, requires superior aerodynamic performance (high L/D) at low Reynolds numbers as well as efficient light-weight structures. These high performance requirements inevitably lead to flexible, high aspect ratio wings that are susceptible to aeroelastic instabilities such as flutter and the adverse impact of large deformations on flight handling qualities.

In Part I, the feasibility of conventional configurations (unswept wings with empennage) as potential HALE solutions was investigated. Flying-wing configurations, as shown in Fig. 1, have also been proposed as alternative design choices for high altitude station keeping missions. High aerodynamic performance may be potentially achieved due to reduced wetted area and intersection drag contributions. However, wing sweep (needed to maintain stability and trim) has a major impact on the overall design. In the low Reynolds number regime, cross-flow instability (a consequence of wing sweep) if not accounted for in the design process presents a potential risk and may disrupt intended transition behavior, resulting in a dramatic loss of aerodynamic performance.

Additionally, aeroelastic instability issues are exacerbated for the flying-wing configuration. The airframe, as a result of wing sweep, is prone to Body-Freedom-Flutter (BFF) which is an aeroelastic instability arising out of the coupling between the short-period mode and the structural bending mode. The absence

*Airframe Technical Lead, AIAA Member.

[†]Aerospace Engineer, AIAA Member.

[‡]Aerospace Engineer, AIAA Member.

of an empennage results in a low pitch inertia leading to an increase in short-period frequencies that may approach the bending mode frequencies. In addition, due to the reduced overall aerodynamic damping of the airframe, the wing bending frequencies are reduced. Wing sweep couples bending and torsion resulting in the blending of airframe pitch and bending modes. In effect, the frequency coalescence and modal blending causes a strong instability with a potency to drive overall aircraft design. Passive means to mitigate this instability by increasing wing stiffness may result in a significant weight increase.² Better success may be achieved using active flutter suppression methods. However, practical realizations of these systems, especially for BFF suppression, are still in their nascent stages although research programs have recently been initiated to mature this technology. Note that aeroelastic issues are less critical for conventional configurations.

Many challenges associated with active controls for flying-wings have been identified in the literature. Structural frequencies are typically low enough to interact with the rigid-body flight dynamic modes and therefore flutter suppression is a challenge due to spillover effects onto the rigid-body dynamics. Other challenges common to high aspect ratio airframes include: designing robust controllers for large model dimensionality, aeroelastic nonlinearities and model uncertainty. Large dimensionality of the aeroservoelastic system may be problematic to maintain state consistency across the flight envelope.³ In addition, statespace control solutions for large order models may lead to implementation issues such as controller fragility.⁴ Several solutions have been proposed to mitigate these issues. References 5,6 demonstrate the use of robust H_∞ control tools applied to BFF suppression. An adaptive distributed sensing and control strategy that isolates the flutter mode for suppression is demonstrated in Ref. 7. This feature enables the use of active flutter suppression alongside existing primary control systems with minimal coupling. Ref. 8 shows the use of a classical control approach using the Identically Located Force and Acceleration (ILAF) sensing/actuation technique.

Several past and ongoing aircraft programs have investigated and built flying-wing aircraft. Some of the earliest examples of flying-wing designs are the Horten sailplanes⁹ of the 1940s. The designs showed a lightly damped pitch response. Flutter events were also reported during flight tests. Another similar configuration is the SB-13¹⁰ which showed typical body-freedom-flutter type instability. Alleviating flutter by increasing the bending stiffness resulted in a significant weight increase. A more recent example is NASA's Environmental Research Aircraft and Sensor Technology (ERAST) program that developed the solar-powered Helios prototype.¹¹ Helios featured an unswept flying-wing configuration with low wing loading. The airframe suffered a fatal crash over the Pacific Ocean on June 26, 2003 due to aeroelastic stability issues. The aircraft had morphed into a high dihedral shape following a gust onset that resulted in an unstable pitch mode. The crash report identified the cause as a lack of adequate analysis tools, in particular, capabilities to model the impact of large wing deformations on flight dynamics. Another recent example is Lockheed Martin's X56 Multi-Utility Technology Test Bed (MUTT)¹² that was developed to demonstrate active flutter suppression and gust load alleviation techniques. The X56 is a small 27.5 ft (span) flying-wing aircraft that shows BFF behavior within the flight envelope. The mini-MUTT,¹³ modeled after the X56, was developed by the University of Minnesota for BFF suppression research. The most recent example is Facebook's Aquila program¹⁴ that demonstrated aeroservoelastic stability with two test flights on a 43 m (span) swept-wing aircraft.

Past developments on large-aspect ratio flexible flight vehicles point to the critical necessity of analysis tools with capabilities to model nonlinear aeroelasticity. In response, medium-fidelity tools that are computationally efficient have been developed to address this need. Nonlinear Aeroelastic Trim And Stability of Hale Aircraft (NATASHA)¹⁵ simulates this behavior using nonlinear composite beam theory in conjunction with a strip-method application of the finite-state induced airflow model. Simulation of High Aspect Ratio Airplanes (SHARP)¹⁶ is a similar tool that couples a geometrically-exact composite beam model with an unsteady vortex lattice method. SHARP also has capabilities to model the effects of gusts. ASWING¹⁷ is a comprehensive nonlinear aeroelasticity tool developed by Mark Drela that models beams with nonlinear Euler-Bernoulli beam theory and aerodynamics with an unsteady lifting line formulation. Capabilities to simulate a variety of gusts and control systems are provided as well. ASWING is used in this study due to its wider acceptance in the industry, user-friendly interface and comprehensive modeling capabilities. Part I of this paper provides several validation studies comparing ASWING with higher fidelity tools.

The MDO framework described in Part I of this paper is utilized in this study to investigate potential

benefits and risks of the flying-wing configuration. In particular, the study demonstrates that flying-wing configurations are stiffness-driven, a consequence of the design being strongly influenced by the BFF instability. The remainder of the paper is organized as follows. Section II reviews the framework with additional details and modifications pertaining to the flying-wing. Section III highlights a similar case study as in Part 1 for the flying-wing configuration. The impact of active flutter suppression systems on aircraft design is also assessed.

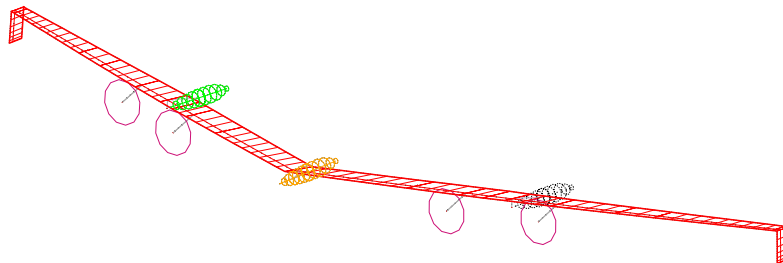


Figure 1. Representative flying-wing configuration under investigation

II. Modeling Formulation

The framework architecture, as shown in Fig. 2, remains essentially the same as that described in Part I of this paper series. However, a few modifications are introduced to handle the impact of wing sweep and the absence of the empennage. In this section we highlight the differences in both modeling and integration of the analysis modules.

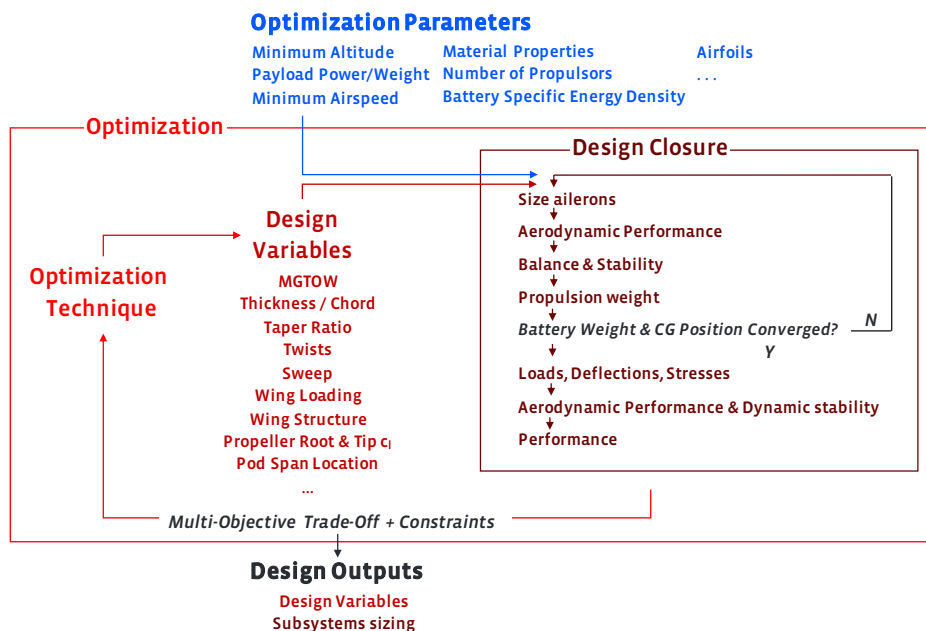


Figure 2. Multidisciplinary sizing and optimization framework flow chart

A. Aerodynamics

The aerodynamic treatment described in Part I is compatible with the introduction of sweep on lifting surfaces. The need to appropriately handle beam deflections led to the use of methods allowing for arbitrary

platform definitions. ASWING is employed to compute the induced flow-field and capture the non-linear coupling between aerodynamics and structures. It uses the extended lifting-line theory of Weissinger therefore accurately capturing the sweep effects on pitching moment. Skin friction and pressure drag components are treated separately.¹⁸ Pressure drag is assumed to scale with the span-wise normal airspeed and the span-normal chord. Skin friction drag is assumed to scale with the local airspeed and local chord (parallel to freestream). For simplicity, no treatment of cross-flow instability driven transition is employed.

B. Structures

The modeling of the swept-wing structure follows a similar approach to that described in Part I. The laminate schedule for the skins and the sparbox also remains the same as that of Part I. Cross-sectional structural properties along the beam axis are computed using Co-Blade²⁰ (classical laminate theory) which are then used by ASWING in its nonlinear Euler-Bernoulli beam theory model. Note that the cross-sections are assumed to be normal to the swept-beam axis. The beam axis is defined herein as the locus of tension centers (as in Part I). Note that for the airfoil shapes and layups considered, the tension, shear and mass centers are nearly co-incidental. The resultant internal loads computed in ASWING are also resolved along the swept beam axis at the corresponding locations where the cross-sectional properties are specified. Similar to the approach describe in Part I, the stresses and strains are then recovered across these cross-sections. Other modeling features such as local buckling are treated similar to Part I.

Note that with this approach and the introduction of wing sweep, the effect of skew-clamping at the wing root is not taken into account. Reference 21 shows that a 10 % discrepancy in wing twist at the tip between Euler-Bernoulli beam theory and finite element shell models may be observed as a result of not accounting for skew-clamping. For large aspect ratios, the discrepancy in tip deflections are relatively insensitive to twist and errors are negligible. Beam theory over-predicts normal stresses by about 10 % and under-predicts shear stresses by 10 % for swept wings. Note that when sizing the structure for strength, the normal stresses typically constrain the design due to the large bending moments incurred at the wing root. However, as will be shown subsequently, the flying-wing configuration is stiffness-driven, and therefore, an accurate prediction of the stiffness distribution is more critical.

The more important effect of wing sweep is the introduction of bending-torsion coupling with implications for aerolastic stability. Also, as aforementioned, the lack of an empennage, leads to the coalescence of the short-period and bending modal frequencies. These conditions create possibilities for flutter to occur within the operating flight envelope. The optimizer therefore seeks to efficiently distribute stiffness and mass across the airframe such that flutter constraints are satisfied.

C. Balance and Stability

The MDO-framework described in Part I (for empennage-stabilized aircraft configurations) sizes the tail area and positions the wing to satisfy pitch trim and static margin requirements respectively. Tail area is specified by an outer optimization loop variable through tail volume. Aircraft static margin is checked and constrained for the deflected shape. Wing position is solved for in the design closure loop by a Newton method. The present variant of the framework follows a similar strategy for flying-wing configurations. Battery mass attached to pods is translated longitudinally to enforce zero pitching moment at the corresponding aircraft CG and wing sweep is optimizer-solved with a constraint on static margin. Both approaches are illustrated in Fig. 3.

The key difference in treatment lies in the computation of the aircraft pitching moment C_M . In the case of empennage-stabilized aircraft, C_M is computed based on the contributions of the wing and tail at their current position and area respectively. It is assumed that wing shape does not change significantly while it is longitudinally displaced. The CG is updated based on the current mass distribution. The wing pitching moment is computed based on its translated value at the new CG from a previous calculation capturing deflections e.g. in polar calculations. The tail contribution is computed using simple relationships at the CG. On the other hand and for flying-wing configurations, the pitching moment C_M is driven to zero directly with ASWING as battery displacement has a significant impact on the wing shape, loading, and pitching moment.

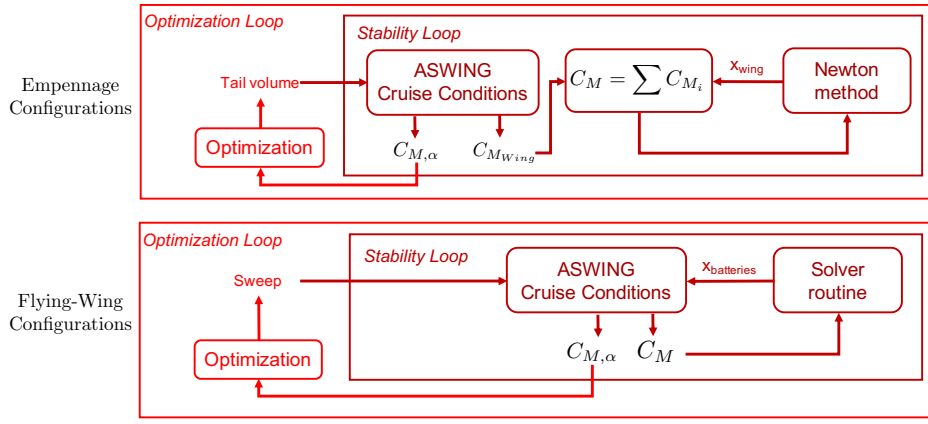


Figure 3. Difference of treatment of aircraft stability treatment between framework versions

Vertical area is provided by downward winglets. Since yawing power is assumed to come from differential thrust, winglet area is sized in the design loop to provide a minimum directional stability C_{n_β} . It is checked for the wing under load and at the accurate CG position.

D. Loads and Dynamics

The loads set used to derive the loads envelope is similar to that of part Part I with the exception of the flying-wing specific worst case gust input parameters described in Table 2. The resulting worst case gust geometries for a representative aircraft are shown in Fig. 4. Note that the strong aeroelastic modal interactions and the resulting marginal flutter instability may lead to longer settling times compared to conventional configurations for given gust excitations. To check for flutter and divergence, an eigenvalue analysis is performed in ASWING for the deformed configuration at the dive speed at several altitudes. The blending between rigid-body modes and structural modes and the deformation under loading complicates the flight dynamics and handling qualities. Accordingly, the behavior of these dynamics may significantly change for different operating conditions within the flight envelope. Static aeroelasticity criteria (torsional divergence and aileron reversal) are also checked with methods similar to that of Part I.

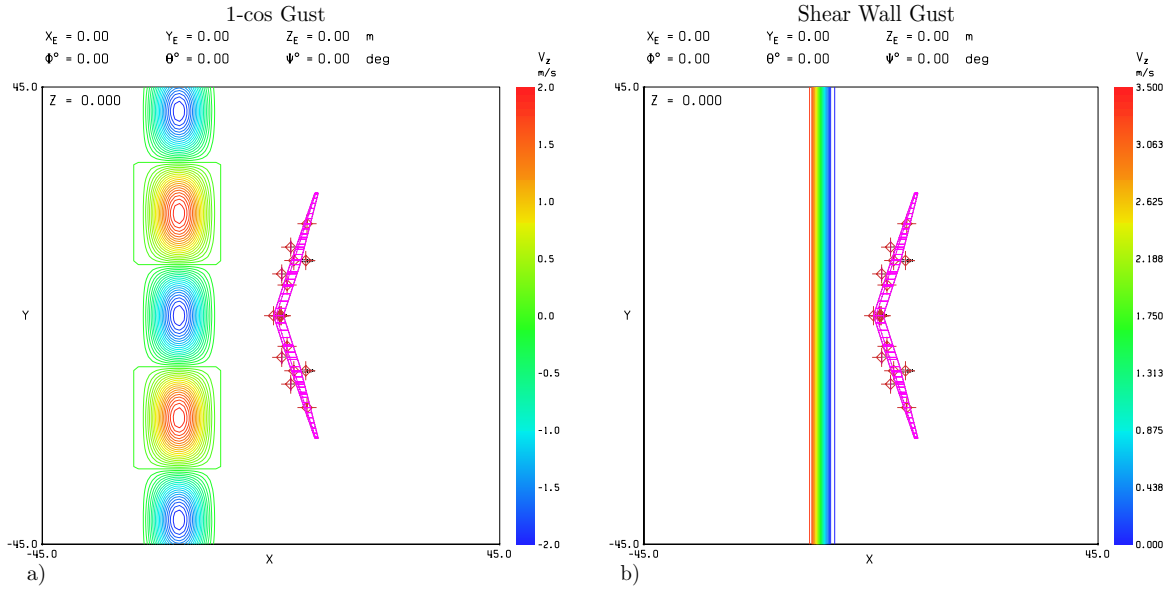


Figure 4. a) Example worst case 1-cos gust, b) Example worst case shear wall gust

E. Controls: Active Flutter Suppression

As discussed previously, BFF instability strongly drives overall design. Accordingly, the impact and potential benefits of active flutter suppression techniques is investigated based on recent results. Three control strategies designed specifically for BFF are considered for this purpose (briefly reviewed in Section 1): 1) Identically Located Acceleration and Force (ILAF)⁸ 2) H_∞ Robust Control⁵ and 3) Modal Isolation and Damping for Adaptive Aeroservoelastic Suppression (MIDAAS).⁷ To incorporate these strategies into the framework from a conceptual perspective, the effect of active suppression on modal stability is captured in terms of extending the stable flight envelope. On average, the three flutter suppression strategies extend the flight envelope by 30 %. Accordingly, constraints on modal stability are set in the framework such that the optimizer guarantees stability for part of the flight envelope, up to 76 % V_{max} . Active controls are then assumed to extend the stable boundary up to V_{max} .

III. Case Study

In order to evaluate the merit of this proposed configuration, multidisciplinary optimization studies are performed to arrive at the minimum cost airplanes of maximum utility. Aircraft mass is used as a proxy for cost, and the extent of the latitude band the solar-powered design can operate in defines usefulness. At a given latitude, the aircraft must fly faster than a given wind speed in order to station-keep. Like in Part I the average 99th percentile wind speed across longitudes is arbitrarily used and the worst case between southern and northern hemisphere limits is taken (see Fig. 5). The framework is ported to modeFrontier®,²² a process-integration and optimization environment. A genetic optimization routine is then used to explore the design space and to derive the Pareto frontier. 150 generations are run with an initial population size of 230 (over 10 times greater the number of optimization variables).

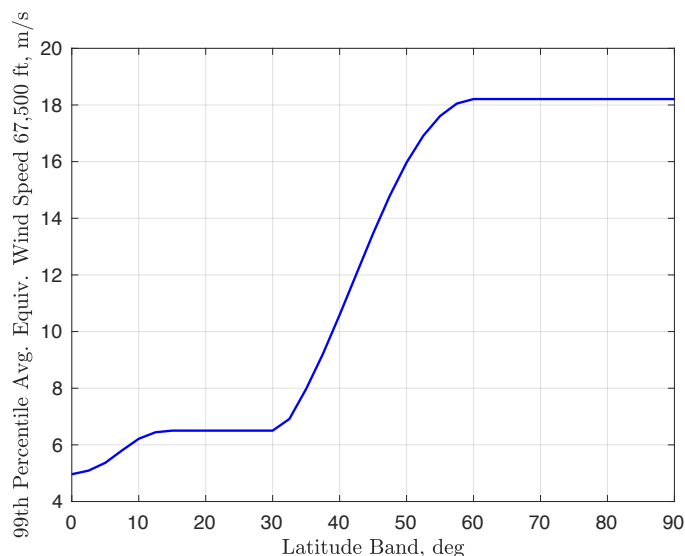


Figure 5. Minimum required aircraft EAS at 67,500 ft to overcome average 99th percentile wind speed

The configuration as shown in in Fig. 1, consists of two propulsion system pairs. A battery pod is positioned between each pair on either wing. Downward winglets are attached to the wingtips to provide directional stability as well as to prevent shadowing effects on the solar cells. The avionics mass model inputs were updated for this configuration, relative to Part I, to reflect the lack of a harness run to the tail(s), the lack of tail servos and an up-sizing of the wing servos to support active flutter suppression. Updated avionics mass inputs are shown in Table 1. Utilizing the present structural parameterization, the optimization routine is able to drive towards feasible solutions against body freedom flutter, here driving the design. The framework’s ability to optimize the number of UD plies in the spar-caps elevates the bending natural frequencies relative to the short period. The aircraft mass distribution is controlled by

the placement of the battery pods and the variables that govern the wing structural layout. Wing sweep controls the amount of bending-torsion coupling that gives rise to the BFF phenomenon as well as aircraft static stability. The optimizer then trades the high-level objectives (weight, latitude) against several design constraints: modes, stresses, stability, etc. To the best of the authors knowledge, no other previous study exists that utilizes global optimization techniques applied to an integrated suite of comprehensive models (low Reynolds number aerodynamics, composite structures, nonlinear aeroelasticity, integrated performance) for swept-wing solar-powered aircraft.

Parameter	Value
Flying-Wing MGTOW Scaled Avionics Mass	0.0093 kg/kg_{MGTOW}
Flying-Wing Span Scaled Avionics Mass	0.12 kg/m
Flying-Wing Fixed Avionics Mass	10.5 kg

Table 1. Flying-wing configuration avionics inputs

Parameter	Value
1-cos Gust Vertical Magnitude	2 m/s
1-cos Gust Span Relative Wavelength	0.833 * Span
1-cos Gust Chord Relative Width	(8 - .167 * Sweep(deg)) * Reference Chord
Shear Wall Gust Vertical Magnitude	3.4 m/s
Shear Wall Gust Relative Chordwise Width	(1 + .5 / 18 * Sweep(deg)) * Reference Chord
Minimum Aeroelastic Modal Damping Ratio	0.3 %

Table 2. Flying-wing worst case gust inputs

Results

Parameter	Value
Payload Mass	10 kg
Payload Power	150 W
Avionics Power	211 W
Minimum Cruise Altitude	67,500 ft
Maximum Altitude	85,000 ft
Battery Specific Energy Density (Cell Level)	400 Wh/kg
Solar Cell Efficiency	23.0 %
Solar Cell Density	0.3 kg/m^2

Table 3. Key optimization parameters (subset)

Key optimization parameters are shown in Table 3 and are equal to the values provided in Part I. The remaining parameters are also kept equal with the exception of the avionics inputs provided in Table 1 and the gust loads input parameters provided in Table 2.

The Pareto frontier of the problem constitutes the set of minimum weight aircraft capable of closing the energy cycle through a given latitude band (see Fig. 6). It is provided for flying-wing configurations with Active Flutter Suppression (AFS) and without. In both cases, the constraints associated with aeroelasticity (worst mode damping through the envelope and torsional divergence margin) were broken over three times more often than the constraints associated with maximum stress. This indicates the problem is stiffness-driven. Sample optimal designs from the frontiers associated with a 20 deg latitude band are shown in Table 4. As expected and similarly to configurations investigated in Part I aircraft MGTOW increases

monotonically with latitude due to the increasing length of night. The sharp increase in weight beyond 30 degrees latitude corresponds to the large increase in wind speed.

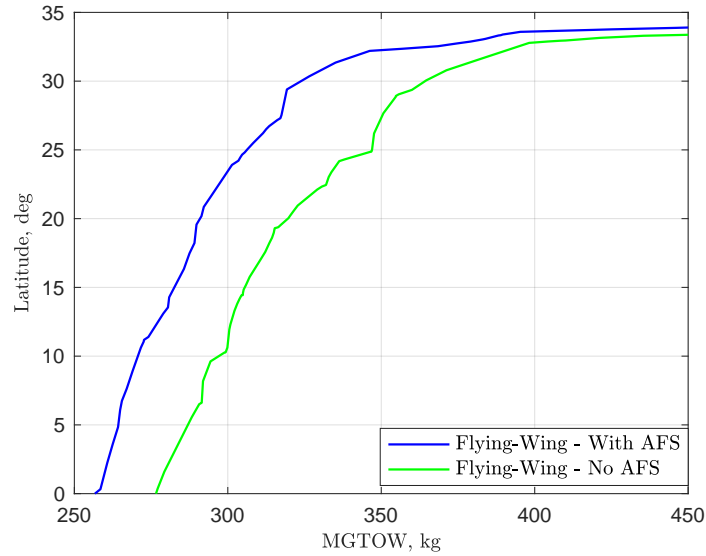


Figure 6. Latitude-aircraft weight Pareto frontier for flying-wing aircraft

Variable	Flying-wing without AFS	Flying-wing with AFS
$MGTOW$	320 kg	290 kg
Sweep angle	17.7 deg	20.4 deg
S_{wing}	77.7 m ²	75.2 m ²
AR	28.4	31.6
$W_{batteries}/MGTOW$	44.1 %	41.4 %
C_L^{cruise}	1.20	1.15
Cruise EAS	7.43 m/s	7.34 m/s
$C_L^{3/2}/C_D$ at cruise	39.8	40.8

Table 4. Design variables for optimal designs at 20 deg latitude

The eigenvalue trajectories for increasing airspeeds are shown in Fig. 7 at an altitude of 26 km (maximum altitude) for both cases: with and without the use of AFS. Without AFS, flutter occurs near the dive speed (10.5 m/s EAS), suggesting that the flutter constraint is dominant. The flutter frequency is approximately 1 Hz. Incorporating AFS, the open-loop flutter speed is reduced to 8 m/s (EAS) with a flutter frequency of 0.8 Hz. Note also that the reduced flutter speed is accompanied by a reduction in the frequency separation between the short-period and the 1st bending mode. The relatively larger frequency separation without AFS is achieved by increasing the sparbox width by approximately 30%. This results in an increased bending structural frequency relative to the short-period mode. However, a consequence of the stiffened structure is a 10% increase in weight. Therefore, it may be concluded that typical active flutter suppression solutions will lead to a 10% more weight-efficient solution over the passive approach for this configuration. The significant weight reduction is again indicative of the dominance of BFF on the design.

Examining the mode shape for the 1st bending mode trajectory confirms that the instability is characteristic of BFF. Figure 8 illustrates the mode shape having both structural flexibility and rigid-body pitch components. In addition to the BFF mode, the first torsion branch also becomes unstable near the same velocity although at a higher frequency. Figure 9 shows the flutter envelope (Altitude vs EAS) for both cases. Although the trends remain fairly similar, the open-loop flutter speeds when using AFS is signifi-

cantly reduced. The envelope was generated by assessing the eigenvalues for the trimmed configuration on a grid of operating points. Stable and unstable regions are then determined.

For both cases, the optimizer placed the battery-pod locations aft of the wing feathering axis while also moving the sparbox closer to the wing quarter-chord. Moving pod masses further forward is generally beneficial to mitigate flutter, however, note that the pod location is a result of the trade between mass distribution, loading, trim and overall aerodynamic performance. The optimizer placed the sparbox close to the quarter-chord for both the flying-wing and empennage configurations in order to minimize aerodynamic coupling.

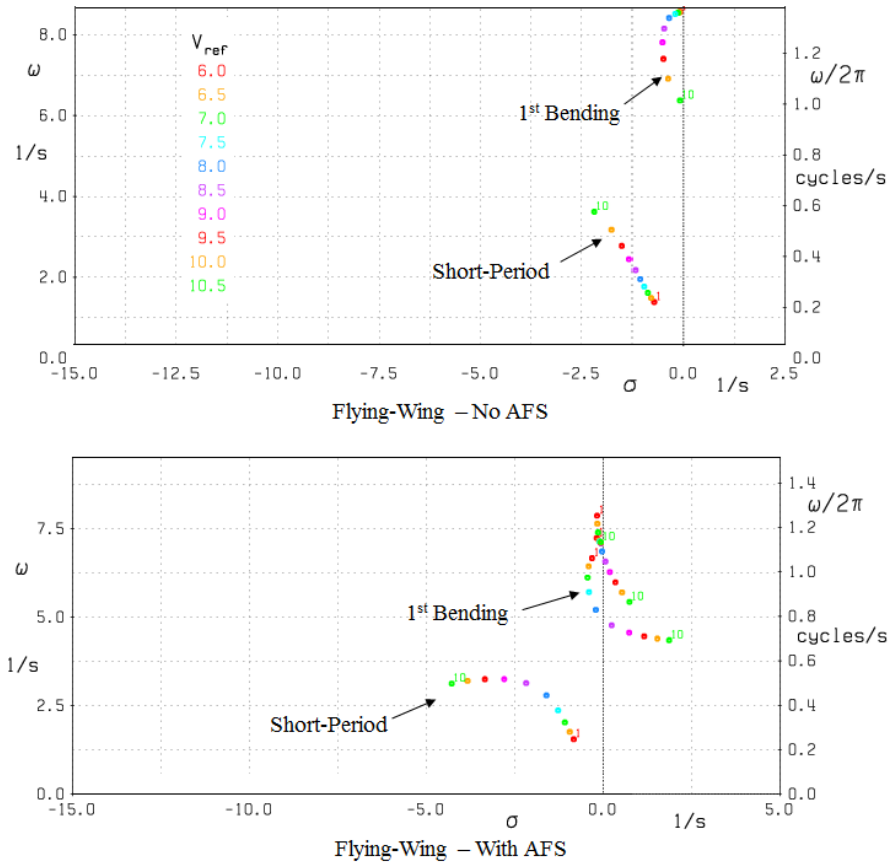


Figure 7. Root locus plot showing onset of body-freedom-flutter

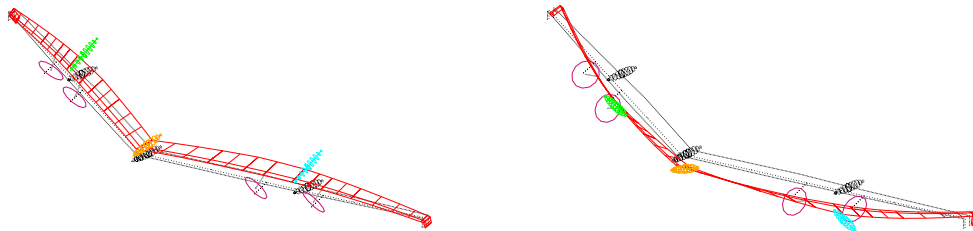


Figure 8. Typical body-freedom-flutter mode shape

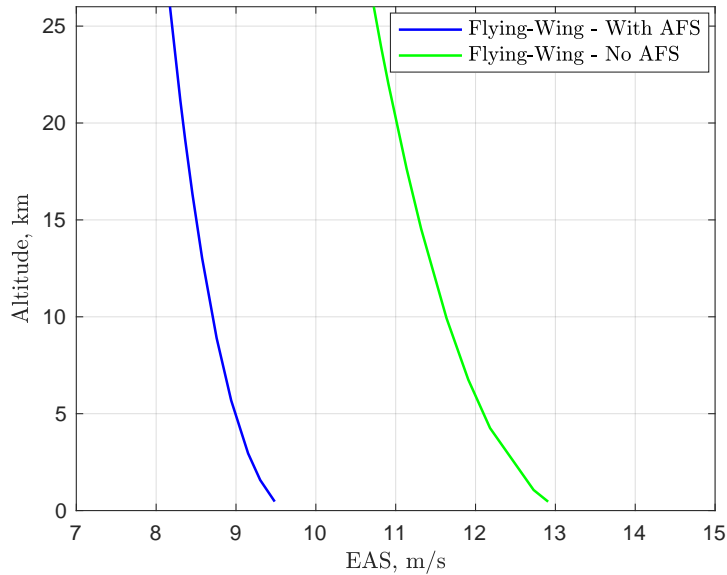


Figure 9. Flutter speed vs altitude

IV. Conclusion

A first-principles approach towards the modeling and design of solar-powered flying-wing configurations was presented. This approach is comprehensive in that it involves several disciplines that are critical to HALE aircraft: Low Reynolds number aerodynamics, design for composite structures, nonlinear aeroelasticity, integrated vehicle performance, etc. Optimization results showed that the flying-wing configuration is stiffness-driven due to influence of body-freedom-flutter on the design. Studies showing the influence of typical active flutter suppression methods were also conducted. As shown, AFS has the potential to decrease aircraft mass by up to 10%. A more comprehensive implementation of the control design strategy will be beneficial to more accurately assess the extent of the envelope expansion and corresponding aircraft mass reduction. Another area for improvement is a more accurate treatment of boundary layer stability, specifically cross-flow based transition due to the inherent spanwise flow that develops over swept wings. Lastly, although preliminary validation (deflections and stresses) for swept-wing structures is provided in Ref. 21, the local buckling criterion needs to be evaluated for this case, and if required, updated to handle wing sweep.

References

- ¹Colas, D. F., Roberts, N. H., and Suryakumar V. S., "HALE Multidisciplinary Design Optimization Part I: Solar-Powered Single and Multiple-Boom Aircraft", 2018 Aviation Technology, Integration, and Operations Conference, 2018 AIAA Aviation, Atlanta, Georgia, 2018
- ²Love, M., Zink, P., Wieselmann, P., and Youngren, H., "Body Freedom Flutter of High Aspect Ratio Flying Wings", 46th AIAA/ASME/ASCE/AHS/ASC Structures, Structural Dynamics and Materials Conference Austin, Texas, April 2005
- ³Ouellette, J., "Aeroservoelastic Modeling of Body Freedom Flutter for Control System Design", Aerospace Controls and Guidance Systems Committee Meeting, March 29-31, 2017
- ⁴Keel, L. H. , and Bhattacharyya, S. P., "Robust, optimal, or fragile?", IEEE Transactions on Automatic Control, 42(8):1098 - 1105, 1997
- ⁵Theis J., Pfifer H., and Seiler, P. J., "Robust Control Design for Active Flutter Suppression", AIAA Atmospheric Flight Mechanics Conference, AIAA SciTech Forum, (AIAA 2016-1751)
- ⁶Hjartarson, A., Seiler, P. J., and Balas, G. J., "LPV Aeroservoelastic Control using the LPVTools Toolbox, AIAA Atmo-

spheric Flight Mechanics Conference, 2013

⁷Danowsky, B. P, “Flutter Suppression of a Small Flexible Aircraft using MIDAAS”, AIAA Atmospheric Flight Mechanics Conference, AIAA AVIATION Forum, (AIAA 2017-4353)

⁸Schmidt, D. K, “Stability Augmentation and Active Flutter Suppression of a Flexible Flying-Wing Drone”, Journal of Guidance, Control, and Dynamics, Vol. 39, No. 3 (2016), pp. 409-422.

⁹Nickel, K., and Wohlfahrt, M., “Tailless Aircraft in Theory and Practice”, American Institute of Aeronautics and Astronautics, Inc., Washington, D.C., 1994

¹⁰Schweiger, J., Sensburg, O., and Berns, H.J., “Aeroelastic Problems and Structural Design of a Tailless CFC Sailplane, 2nd International Symposium on Aeroelasticity and Structural Dynamics, Aachen, Germany, April 1985

¹¹Noll, T. E., Brown, J. M., Perez-Davis, M. E., Ishmael, S. D., Tiffany, G. C., and Gaier, M., “Investigation of the Helios Prototype Aircraft Mishap, NASA Report, Jan 2004.

¹²Ryan, J. J., Bosworth, J. T., Burken, J. J., and Suh, P. M., “Current and Future Research in Active Control of Lightweight, Flexible Structures Using the X-56 Aircraft, AIAA SciTech, 2014, doi:10.2514/6.2014-0597

¹³Beranek, J., Nicolai, L., Buonanno, M., Burnett, E., Atkinson, C., Holm-Hansen, B., and Flick, P., “Conceptual Design of a Multi-Utility Aeroelastic Demonstrator, 13th AIAA/ISSMO Multidisciplinary Analysis Optimization Conference, 2010, pp. 21942208.

¹⁴Gomez, M. L, Cox, A., “Flying Aquila: Early lessons from the first full-scale test flight and the path ahead”, <https://code.facebook.com/posts/268598690180189>, Retrieved: April 4 2018

¹⁵Patil, M. J., Hodges, D. H., and Cesnik, C.S., “Nonlinear aeroelasticity and flight dynamics of high-altitude long-endurance aircraft”, Journal of Aircraft, Jan 2001.

¹⁶Murua, J., “Flexible Aircraft Dynamics with a Geometrically-Nonlinear Description of the Unsteady Aerodynamics”, Ph.D Dissertation, Imperial College, May 2012.

¹⁷Drela, M., “Integrated Simulation Model for Preliminary Aerodynamic, Structural, and Control-Law Design of Aircraft”, AIAA Paper 99-1394, AIAA 40th SDM Conference, St Louis, April 1999.

¹⁸M. Drela., “N3 Aircraft Concept Designs and Trade Studies Appendix”, Technical Report NASA CR-2010-216794/VOL2, NASA, 2010.

¹⁹Drela, M., “Integrated Simulation Model for Preliminary Aerodynamic, Structural, and Control-Law Design of Aircraft”, AIAA Paper 99-1394, AIAA 40th SDM Conference, St Louis, April 1999.

²⁰Sale, D., Aliseda, A., Motley, M., and Li, Y., “Structural Optimization of Composite Blades for Wind and Hydrokinetic Turbines”, Proceedings of the 1st Marine Energy Technology Symposium METS 2013 April 10-11, 2013, Washington, D.C

²¹Dorbath, F., Nagel B., and Gollnick V., “Comparison of Beam and Shell Theory for Mass Estimation in Preliminary Wing Design”, 2nd Aircraft Structural Design Conference, 26-28 October 2010

²²ESTECO s.p.a., modeFrontier 4 User Manual, 2011.